Materials Advances

ROYAL SOCIETY OF CHEMISTRY

PAPER

View Article Online
View Journal | View Issue

Cite this: *Mater. Adv.*, 2025, **6**, 6856

Biowaste-derived carbon as an electrode material for sodium batteries and capacitors

Chandra Sekhar Bongu and Edreese H. Alsharaeh *

The conversion of inexpensive, plentiful, and renewable biomass into porous carbon materials for use in sodium-ion batteries and supercapacitor electrodes has garnered attention in recent years. This study presents a novel approach where blackberry seeds were carbonized and chemically activated with potassium hydroxide (KOH) to form activated carbons (ACs). The synthesized blackberry seed-derived activated carbon (BBSDAC's) morphology, defectiveness, crystal structure, and textural characteristics were characterized using scanning electron microscopy (SEM), Raman spectroscopy, X-ray diffraction (XRD), and low-temperature nitrogen physisorption. The characterization confirmed that the biocarbon has a good surface area with micropores and defectiveness. The electrochemical performance of the sodium-ion energy storage of the biocarbon was investigated in a half-cell, yielding a discharge capacity of 322 mAh g^{-1} at a rate of 100 mA g^{-1} with good rate capability, as well as outstanding cycling stability, retaining 99% of its capacity after 200 cycles. Even after 10 months of rest, the cell showed no capacity decay. Additionally, activated carbon was investigated in an aqueous solution as an electrode material for sodium-ion capacitors. The BBSDAC 700 exhibits remarkable characteristics with a high specific capacitance of 218 F g^{-1} at a current density of 1 A g^{-1} and excellent cycling stability with around 99.0% coulombic efficiency after 10 000 cycles. The capacitor demonstrated an energy density of around 20 Wh kg^{-1}. The findings show that the BBSDAC 700 electrode advances the electrode materials used in energy storage applications.

Received 6th April 2025,
Accepted 4th August 2025

DOI: 10.1039/d5ma00333d

rsc.li/materials-advances

1. Introduction

It is necessary to appropriately use energy from renewable sources to reduce the gap between energy generation and demand. In particular, fossil fuels, the primary source of energy generation today, are overused due to the constantly rising demand for energy brought on by population increase and industrial modernization.[1] Nowadays, the effects of global warming are visible as a result of increased air pollution brought on by the overuse of fossil fuels. In order to achieve a clean and sustainable environment, energy from renewable sources needs to be effectively stored and used when needed. Energy storage comes in various forms, including mechanical, electrochemical, and thermal.[2] The electrochemical energy storage system is one of the most important in appliances and consumer electronics. Batteries and supercapacitors are the most widely used electrochemical energy storage devices. Because of its exceptional coulombic efficiency, high energy, and high cell voltage, the lithium-ion battery (LIB) has dominated the portable consumer electronics market during the last twenty years.[3] The LIB's appealing qualities make it a viable option for use, even in electric cars. However, such implementation for large-scale grid integration and e-vehicles is constrained by the limited lithium resources.[4] Therefore, it is essential to develop further dependable battery technologies. Electrochemical sodium-ion storage technology is one of the other choices.[5–7] Since sodium is the fourth most prevalent element on Earth and is abundant in salt water, it may find application in e-vehicles and large-scale grid integration.[8] However, the solution to bringing sodium-based batteries to market is the creation of inexpensive, high-performing electrode materials. Given that the sodium content of seawater can reach 60% and the estimated 2.6% total sodium reserves in the Earth's crust, sodium is far more affordable than lithium.[9,10] The development of sodium ion battery (SIB) technology is therefore acceptable.

With a sodium electrolyte, a conventional SIB has sodium metal as the anode and a sodiated transition metal oxide as the cathode. The SIB and LIB have nearly identical chemistry, making it advantageous to investigate creating a dependable sodium-ion storage device. However, the secret to bringing sodium-based batteries to market is the creation of inexpensive, high-performing electrode materials. Several high-performance cathode materials for SIBs have been identified, including phosphates, sulfates, Prussian blue, and layered oxides.[11–22] Furthermore, various anode materials, such as alloys, oxides, organic compounds, and carbon materials, have been extensively researched for SIBs.[23–36] Rapid capacity fading and the

College of Science and General Studies, AlFaisal University, PO Box 50927, Riyadh, 11533, Saudi Arabia. E-mail: ealsharaeh@alfaisal.edu

loss of electric contact result from the alloy anodes' significant volume expansion during sodium insertion. Oxide anodes have very low capacities.[37–42] Among these, the carbon anode is appealing because of its price and ease of generation. The Na^+ radius (1.02 Å) is greater than that of the Li^+ ion (0.76 Å), making graphite, the typical anode for the LIB, unsuitable as an anode for SIBs. Due to its ordered layer structure and basal length of around 0.34 nm, graphite is not conducive to large-scale Na^+ intercalation.[43,44] The Na^+ intercalation requires a minimum intercalation distance of 0.37 nm. Therefore, restricted Na^+ intercalation into graphite layers frequently leads to low reversibility and it cannot be used as an SIB anode material.[45,46]

Carbonaceous anode materials derived from biomass sources have become more and more popular recently because of their availability, affordability, accessibility, and environmental friendliness.[47] However, carbons generated from biomass have high surface area, high porosity, and superior electrical conductivity, making them ideal for storing sodium ions.[48] The biomass-derived carbonaceous materials from rice husks,[49] apple,[50] coconut shell,[51] corncob,[52] bamboo and wood,[53,54] cork-derived carbon,[55] algae-derived hard carbon,[56–58] coffee derived carbon,[59] and sugarcane[60] have gained much attention in SIBs due to their extreme electrochemical properties. As a result, biomass utilization has received a lot of interest in energy storage research.

It was discovered recently that disordered carbon has good reversibility in sodium-ion storage. There are various ways that disordered carbon can be produced. By carbonizing the male inflorescence of Borassus flabellifer, for example, Thileep Kumar *et al.* produced hard carbon with a practical capacity of 413 mAh g^{-1}.[61] According to He Chen *et al.*, pitch-derived carbon had a specific capacity of 312 mAh g^{-1}.[62] Chenrayan Senthil *et al.* produced carbon using nitrogen self-doped activated carbon obtained from seaweed and reported a specific capacity of roughly 303 mAh g^{-1}.[47] It was determined that the supply of carbon and the method of activation to produce disordered carbon had a significant impact on the sodium-ion performance.[63]

Recently, there has also been an increase in interest in creating sodium-ion capacitors (SICs) in addition to SIBs due to many features such as capability to discharge at high power, long cycle-life and low cost. It is possible to create an SIC using either aqueous or nonaqueous electrolytes in symmetric or asymmetric arrangements. In 2012, in the first report on SICs, commercial activated carbon was used as the positive electrode and commercial hard carbon as the negative electrode. SICs are often manufactured in a variety of forms, including symmetric, asymmetric, and hybrid capacitors, where the electrolyte medium is a solution containing sodium salt. Therefore, the electrolyte serves as both the source of Na^+ ions and their conducting medium. Carbonaceous materials, such as graphene oxide, graphene, aerogels, carbon nanotubes (CNTs), activated carbon (AC), carbon black, *etc.*, are being investigated as capacitor electrode materials. For instance, Yunchao Li *et al.* produced activated biocarbon from bamboo chips and reported a specific capacitance of 208 F g^{-1} at a current density of 1 A g^{-1}.[64] Yong Yao *et al.* prepared a carbon material from red dates and reported a specific capacitance of 341.9 F g^{-1} at a current density of 0.5 A g^{-1}.[65]

Biomass is the ideal carbon source for carbon-based electrodes since the sustainable development goals state that electrode material manufacturing must adhere to sustainability standards. Ranjith *et al.* reported a specific energy of 118 Wh kg^{-1} after fabricating an SIC with biocarbon produced from cinnamon sticks as the anode.[66] Sara Paya *et al.* created an S-doped carbon sponge that may deliver a specific capacitance of 58 F g^{-1} at 0.1 A g^{-1} when utilized as an electrode for SICs.[67]

The little fruit known as the blackberry, or jamun, is undervalued despite having substantial nutritional and therapeutic significance. Fruit is a great source of anthocyanins, vitamins, minerals, pectin, and antioxidants.[68,69] Having originated in Indonesia and India, it is found all over Southern Asia and grows well in tropical and subtropical environments. Nonetheless, blackberry seeds are used in traditional medicine to cure a variety of conditions, such as inflammation, cough, and diarrhea.[70,71] The most significant usage of blackberry seeds is in the treatment of diabetes. One plant yields around 400 000 blackberry seeds annually. In the food sector, blackberry seeds are often removed during processing. The seed oil is made from blackberry seeds, and blackberry seed flour is a by-product of the oil production process. As far as we know, no publications have been found using disordered carbon generated from blackberry seed biomass as the electrode material for SICs and SIBs. As a result, the current study investigated using disordered carbon extracted from the biomass of blackberry seeds as the electrode material for SIBs and SICs. This study used a widely established two-step procedure that included carbonization and KOH activation steps to synthesize BBSDAC from blackberry seeds. XRD, transmission electron microscopy, scanning electron microscopy (SEM), Raman spectroscopy, BET, cyclic voltammetry, and galvanostatic charge–discharge tests were used extensively to characterize the synthesized BBSDAC. Both an SIB and SIC were used to measure the BBSDAC's electrochemical performance. The BBSDAC disordered carbon material exhibits a high capacity, outstanding rate performance, and steady cycling performance when used as an anode material for SIBs. Even after 100 cycles, its specific capacity can remain at 310 mAh g^{-1} at a current density of 100 mA g^{-1} and 225 mAh g^{-1} with a current density of 500 mA g^{-1}. The BBSDAC demonstrated outstanding long-term cycling stability for up to 10 000 cycles in SICs, with a high energy density of around 20 Wh kg^{-1} and a high-power density of over 726 W kg^{-1}.

2. Experimental section

2.1. Materials

All the chemicals used in the manuscript were purchased from LabChem and Sigma Aldrich without further purification. To prepare the carbon material, blackberry seeds are gathered from the local fruit vendor market, cleaned with triple-distilled water, and then used.

2.2. Synthesis of BBSDAC

The following is the production process for the biocarbon derived from blackberry seeds. After being gathered at a nearby

market, the blackberry seeds were cleaned with triple-distilled water and dried at 150 °C in an oven. 10 g of the dried blackberry seeds were pre-carbonized in a muffle furnace for 3 h at 350 degrees Celsius in the air. In a nitrogen environment, the pre-carbonized seeds were crushed, combined with KOH (1 : 3), loaded into an alumina boat, and heated for 3 h at 700 °C at 5 °C min^{-1}. After continuously washing the resulting black powder in a 1 M HCl solution with triple distilled water to remove impurities and reach a neutral pH, the final BBSDAC product, a dry powder, was produced. At 80 °C, the black powder was subsequently vacuum-dried. The synthesized carbon powder was identified as BBSDAC-700 and underwent several characterization tests.

2.3. Material characterizations

The sample's X-ray diffraction was recorded using a Bruker D8 Advance X-ray diffractometer and Cu-K radiation (λ = 1.5406 A°). An excitation energy of 2.33 eV and green laser light (λ = 532 nm) were utilized to get Raman spectra (WITec Raman spectroscopy). Both a transmission electron microscopy (TEM) (JEOL-JSM-700F) and a field emission scanning electron microscopy (SEM) (JEOL-JEM-2011(200KV)) system were used to image the materials. The BBSDAC material's mean pore width and specific surface area were determined using the Brunauer–Emmett–Teller (BET) and Barrett–Joyner–Halenda (BJH) methods (Autosorb iQ, Quantachrome, USA).

2.4. Electrochemical characterizations

2.4.1. Sodium-ion battery characterization. Sodium ion storage of the BBSDAC 700 electrode was investigated using a CR-2032 type cell with sodium metal as a counter and reference electrode. First, a 70 : 20 : 10 weight ratio was used to combine the BBSDAC 700 sample, super p carbon, polyvinylidene difluoride (PVDF) binder, and *N*-methyl-2-pyrrolidone (NMP) solvent to create the working electrode slurry. The doctor blade method was used to apply the produced slurry to copper foil, and it was vacuum-oven dried for 12 h at 80 °C. Next, a 15 mm disc was perforated with the BBSDAC 700 coated copper foil to serve as the working electrode with a mass loading of the active material of 1–1.2 mg. In an argon-purged glovebox (MTI corporation), the coin cell was put together using Whatman glass filter paper as the separator and 1 M $NaPF_6$ electrolyte in ethylene carbonate (EC) and diethylene carbonate (DEC) (1 : 1 volume ratio). An electrochemical workstation (Biologic VSP) was used to record the cyclic voltammogram (CV) curves on the completed half-cell within the potential window of 0.01–3.0 V at a scan rate of 0.1 mV s^{-1}. Battery testing equipment (Biologic VSP) was used to record the galvanostatic charge–discharge (GCD) profiles on the manufactured half-cell at different current rates with the same potential. Plots of the coin cell's electrochemical impedance were taken before and after cycle life tests. The frequency range in which the impedance graphs were recorded was 10 KHz to 100 mHz with an amplitude voltage of 10 mV.

2.4.2. Sodium capacitor characterization. The slurry mentioned above was used to create the capacitor's electrode. The slurry was evenly spread out on a current collector made of Ni foam. A vacuum was used to dry the BBSDAC 700 coated Ni foam at 80 °C. A three-electrode cell configuration comprising the BBSDAC 700 as the working electrode, platinum (Pt) as the counter electrode, and silver/silver chloride (Ag/AgCl) as the reference electrode in 1 M Na_2SO_4 (aqueous) electrolyte was used to first assess the carbon capacitor research. On the manufactured three-electrode cell design, the charge–discharge curves at various current rates and CV profiles at various scan rates were recorded in the potential range of 0 to 1.2 V. A CR2032-type button cell was used to test the symmetric device performances in an aqueous sodium-ion capacitor employing Whatman glass filter paper as a separator. In the symmetric device, which had two identical electrodes coated with BBSDAC 700, the electrolyte was 1 M Na_2SO_4. The previously mentioned electrochemical workstation was used to record the CV and GCD profiles for capacitors in the potential ranges of 0–1.2 V. The following formula (1) was used to calculate the specific capacitance (F g^{-1}) in a three-electrode arrangement from the galvanostatic discharge curve:

$$C_s = \frac{I\Delta t_d}{m\Delta V} \quad (1)$$

Discharge current (A) = I. Discharge time (s) = Δt. Mass of the active material (g) = m. Discharge potential window (V) = ΔV.

The GCD curves at various current densities might be utilized for calculating the supercapacitor cell's energy density (E, Wh kg^{-1}) at various power densities (P, W kg^{-1}) using eqn (2) and (3):

$$E = \frac{0.5 \times C_{CD} \times (\Delta V)^2}{3.6} \quad (2)$$

$$P = \frac{E}{\Delta t} \quad (3)$$

Potential window of discharge (V) = ΔV. Discharge time (s) = Δt.

3. Results and discussion

3.1. Physical characterization

XRD analysis was performed on the prepared BBSDAC sample, and Fig. 1 shows the produced XRD pattern. Two broad Bragg's peaks, centered at 2θ of 23.4° and 43.7°, are visible in the pattern. According to the standard pattern, these peaks correspond to the (002) and (100) Bragg carbon planes.[72] The existence of single-layer carbon not stacked equally apart, giving the appearance of such prominent peaks, is thought to be more indicative of disordered carbon. The BBSDAC 700 computed *d*-spacing is 0.38 nm, more significant than the graphitic lattice's (0.334 nm), providing plenty of room to utilize it for SIBs further.[73] Additionally, BET analysis was used to examine the BBSDAC 700 sample's surface area and pore size distribution. Fig. 1b and c display the acquired isotherm and pore size distribution curves. The adsorption follows a type IV isotherm. Remarkably, the activated biocarbon has a large surface area of 604 m^2 g^{-1} and pores about 34 nm in size Fig. 1c. The modest activation temperature used may be responsible for the

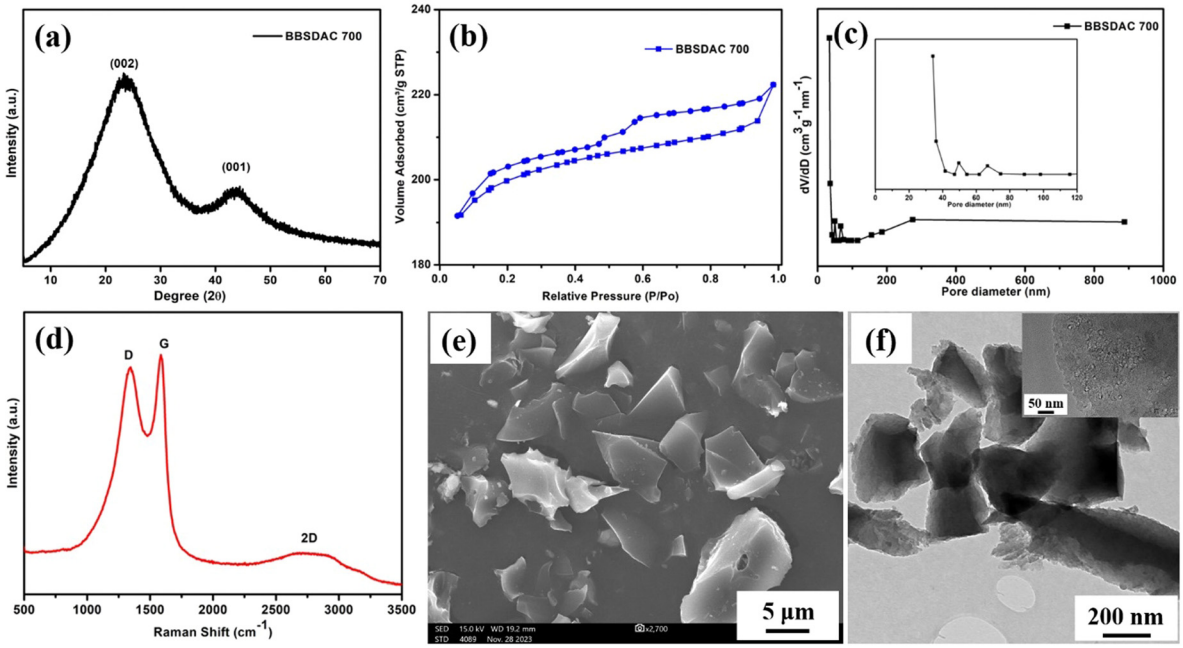

Fig. 1 (a) XRD pattern, (b) N_2 adsorption/desorption isotherm, (c) pore distribution, (d) Raman spectrum, (e) SEM and (f) TEM for the BBSDAC 700.

particular surface area. Most of the cores of activated carbon are mesopores. These mesoporous cores are anticipated to promote rapid ion diffusion, which is necessary to attain high-rate capability.

The structural characteristics of the amorphous materials can be determined with the help of the Raman spectra. Fig. 1d displays the obtained Raman profile. Two significant shifts at 1348 and 1590 cm^{-1} easily differentiate the D and G bands of the BBSDAC 700. The D band represents the sp^2-hybridized mode of the disordered carbon and E_{2g} mode graphitic carbon in the BBSDAC 700.[74] BBSDAC 700's computed I_D/I_G ratio of 0.85, which is less than 1, indicates that partially graphitized disordered carbon is present.[75] The presence of partial graphitization in BBSDAC with intended flaws is confirmed by the graphitic band intensity, which is significantly higher than the defective band in BBSDAC 700. Defective BBSDACs enhance electrochemical behavior, particularly conductivity, charge transfer kinetics, and easy diffusion.[76] On the other hand, the sample's peak at 2777 cm^{-1}, corresponding to the second order of the D band (2D), shows a few graphene layers in addition to the single layer. As a result, the benefit of using BBSDAC as an anode becomes crucial. Transmission electron microscopy (TEM) and scanning electron microscopy (SEM) were used to examine the sample's shape and structure. Fig. 1e shows SEM images of blackberry seeds (BBS) carbonized at 700 °C. The BBSDAC 700 particles retain their irregular forms and smooth surfaces, indicating that the carbonization process at 700 °C has minimal impact on the size and surface morphology of the particles. Fig. 1f shows the BBSDAC 700's TEM images [inset 50 nm image], clearly showing the sample's microstructure. The TEM images clearly show the presence of porous sheets with irregularly sized pores across the carbon sheets. Because gases like H_2O and CO_2 are released during the carbonization process, the TEM image (Fig. 1f) shows a disordered porous network structure. The disordered porous carbon material can offer more efficient ion transfer and electrolyte diffusion space than granular carbon materials. In addition to offering superior mechanical flexibility, the multi-stage pore structure can increase electron transit and sodium ion storage capacity. Additionally, open-framework structures can be mutually bridged, which facilitates electron and ion transmission.[77,78]

3.2. Electrochemical characterization

Cyclic voltammetry (CV), electrochemical impedance spectroscopy (EIS) and cycling investigations of the electrochemical performance of the BBSDAC 700 for the SIB anode were examined with sodium metal serving as the counter and reference electrode and 1 M of $NaClO_4$ dissolved in EC : PC (1 : 1 v/v) solution as an electrolyte. Fig. 2a displays the first five CV curves of the BBSDAC 700 in the potential range of 0.01–3.0 V at a scan rate of 0.1 mV s^{-1}. The modest peak decrease seen in the cycles at about 0.45 V is due to the creation of the solid–electrolyte interface (SEI) layer and an irreversible reaction between the electrolyte and the active material's surface functional groups. As is well known, a low initial coulombic efficiency (ICE) directly results from the SEI layer's creation and other irreversible processes. All five cycles exhibit a sharp cathodic peak and less sharp anodic peaks in the potential window of 0.5–0.02 V, suggesting more sodium ion extraction. The adsorption/desorption of Na^+ into the carbon matrix is responsible for the cathodic and anodic peaks.[63] BBSDAC 700's CV profiles resemble those of disordered carbon compounds that have been previously documented.[79] The cathodic and anodic curves showed no discernible alterations from the second cycle, indicating steady SEI layer development and

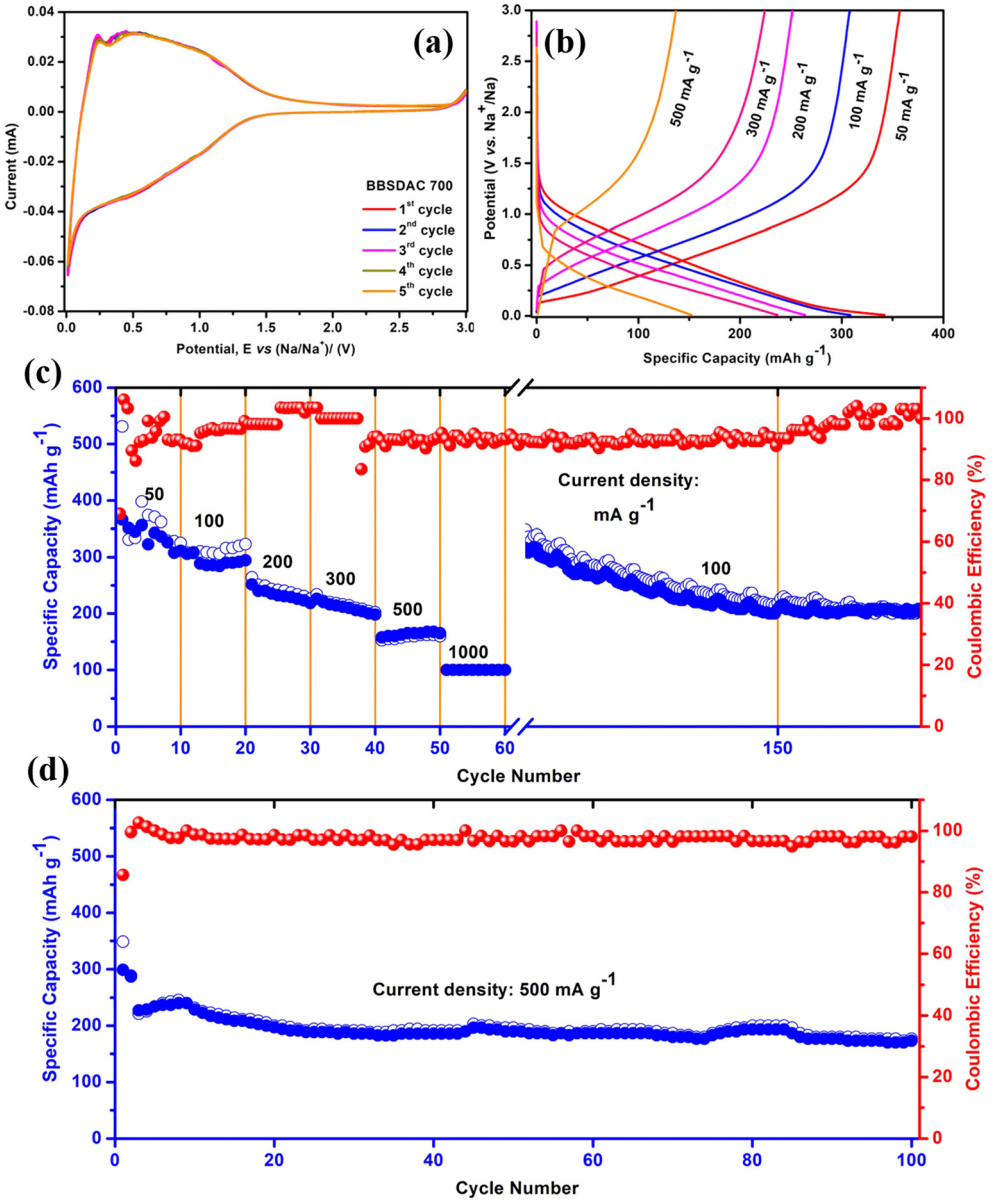

Fig. 2 Electrochemical performance of the half cells. (a) CV curves of the first five cycles at a scan rate of 0.1 mV s^{-1}, (b) charge–discharge profiles with different current density, (c) rate capability and coulombic efficiency at different current density and (d) long-term cycling study and coulombic efficiency at 500 mA g^{-1} of BBSDAC 700.

superior electrochemical reversibility during cycling.[80] Therefore, the CV data verify that the sodium ion can be efficiently intercalated and deintercalated by the disordered carbon produced from the BBSDAC 700.

Fig. 2b shows the GCD profiles recorded at different current rates 50, 100, 200, 300, and 500 mA g^{-1} in a potential window from 0.01–3.0 V *vs.* Na/Na^+. Fig. 2c shows reversible capacities of about 325, 322, 226, 202, 159, and 100 mAh g^{-1} obtained at 50, 100, 200, 300, 500, and 1000 mA g^{-1}, for BBSDAC 700, respectively. Interestingly, these capacities are marginally more significant than those of the matching sodium–metal cell. Since there is no fresh sodium–metal interface exposed during each cycle, the higher capacity is explained by reduced electrolyte degradation. In addition, the mesopore diameter distribution of BBSDAC 700 significantly enhances the sodium storage capacity, facilitating faster sodium ion diffusion and providing a more accessible surface area for sodium intercalation, which leads to improved battery performance (improved rate performance). However, the stable SEI layer formation (Fig. S2) is also crucial for both high-rate performance and reversible capacity. After the rate test, returning to 100 mA g^{-1} yields a capacity of about 388 mAh g^{-1} and is stable up to 200 cycles, indicating the cell's ability to withstand high currents and practical implementation. This demonstrates that the disordered biocarbon produced from BBSDAC 700 can be a desirable anode for SIBs. According to Table 1, a literature review found that carbon from different sources has a discharge capacity less than BBSDAC 700. Unquestionably, compared to many biocarbon reports, the

Table 1 Comparison of the sodium-ion battery based on a carbon anode and the discharge (specific) capacity report

Carbon source	Capacity (mAh g^{-1})	Current density (mA g^{-1})	Cycling stability	Ref.
Seaweed	303	100	100	47
Egg yolks	208	100	200	81
Apple-biowaste	240	50	80	50
Lotus petioles	230	50	200	82
Bamboo leave	200	100	300	83
Renewable cotton	315	50	100	84
Tea-derived carbon	325	28	—	85
Typha	204	100	400	86
BBSDAC 700	**322**	**100**	**200**	**This work**

discharge capacity obtained in this work is more significant. Following the rate performance experiments, the cell was examined for a long cycle with the coulombic efficiencies at 500 mA g^{-1} in the voltage range of 0.01–3.0 V. Fig. 2d illustrates the analysis that was done *vs* Na/Na^+. The first Na^+ intercalation process was observed to deliver a high discharge capacity of 347 mAh g^{-1}, with a comparable charge capacity of 298 mAh g^{-1}, resulting in a high coulombic efficiency of 85%. It is evident that in the second cycle, the coulombic efficiency rises quickly to 98.0%. The BBSDAC 700 anode has outstanding cycling stability from the second cycle onward. Following the 100th cycle, a stable reversible capacity of up to 176 mAh g^{-1} is maintained, and the coulombic efficiency surpasses 99%. The enormous number of accessible pores is responsible for the high capacity. It is well known that some Na ions are deposited within the pores because a specific number of mesopores can hold more Na ions than surface adsorption alone.

The half-cell underwent impedance analysis to comprehend the stability, ion mobility, and reaction kinetics of the BBSDAC 700 electrode. Fig. S1 displays the half-cell Nyquist profile of the BBSDAC 700 electrode before and following cycle life tests. The low-frequency portion of each Nyquist plot is a sloping line, whereas the high-frequency portion is a semicircle. The semicircle represents the electrolyte resistance (R_s) and charge transfer resistance (R_{ct}), and the sloping line represents the Warburg impedance (Z_w) related to the Na-ion diffusion in the BBSDAC 700 anode.[87] It is found that the half-cell typically exhibits just a slight variation in the Nyquist plots, even after 100 charge–discharge cycles. The corresponding circuit is shown in Fig. S1 (inset) fitted to the resulting Nyquist curves. Table 2 displays the fit values. Before cycling, the cell with the BBSDAC 700 electrode had an R_{ct} of 2000 Ω, higher than the cell that had undergone 100 cycles (1596 Ω). This shows that the BBSDAC 700 electrode's electronic conductivity rises when cycling and is not degraded, which agrees with the cell's cycling capabilities.[88,89]

Table 2 R_s and R_{ct} values of the BBSDAC 700 anode before and after cycling

State of the cell	R_s (Ω)	R_{ct} (Ω)
Before cycling	28	2000
After cycling	2.5	1596

Self-discharge was investigated and shown in Fig. 3 to determine the influence of the electrochemical performances of the Na ion battery. The Na ion battery was recharged to 3.0 V after 250 cycles at 100 mA g^{-1} and allowed to rest for 10 months. The CV was run after a ten-month rest of the cell to analyze the electrode stability (Fig. 3a). The irreversible breakdown of the electrolyte, which results in the formation of a stable solid–electrolyte interface (SEI) close to the electrode/electrolyte, is responsible for the broad peak that arises in the cathodic direction at roughly 0.6 V in the first cycle. The well-overlapped CV curves in the succeeding cycles demonstrate that the development of the SEI predominantly happens in the starting discharge phase, which is favorable for the stability of Na insertion/extraction over the remaining scan cycles. After 10 months of rest, the SEI stability of the BBSDAC 700 electrode was studied using Fourier-transform infrared (FTIR) spectroscopy (Fig. S2). The FTIR spectrum reveals large absorption bands in the ranges of 1800–1490, 1435–1320, and 1270–920 cm^{-1}. These bands correspond to the stretching of the O–C–O and C–O bonds, as well as the symmetric/asymmetric stretching of the C═O bond. The carbonate-derived SEI peak at 1765 cm^{-1} is attributed to the stretching vibration of CO_3^{2-}, which results from the decomposition of EC and is responsible for the formation of $(CH_2OCO_2Na)_2$ and CH_3CH_2O-CO_2Na. The inorganic Na_2CO_3 peaks are located at 1482, 1393, and 894 cm^{-1}. The peaks at 551 cm^{-1} are ascribed to the salt of $NaPF_6$. Following rest, the half-cell's Nyquist profile is shown in Fig. 3b. After the rest period, it is observed that the R_{ct} value decreases, suggesting that the electrode has not deteriorated. Fig. 3c depicts the cyclability of the rested SIB after resting for 10 months. Interestingly, even after resting for 10 months, the SIB delivers the capacity of 265 mAh g^{-1} at a current density of 100 mA g^{-1} and exhibits excellent coulombic efficiency of nearly 100%. The results indicate that the electrode BBSDAC 700 is stable after 10 months and has no decomposition in the electrode material.

Activated carbon is used widely in capacitors because of its large surface area, high conductivity, affordability, and capacity for long-term cycling stability. Since carbon materials are often non-faradaic, EDLC production at the electrode/electrolyte interface is the primary method used to achieve charge storage. Activated carbon with a large surface area typically had a high specific capacitance, which led to the testing of BBSDAC 700 for usage as a capacitor in an aqueous sodium electrolyte. A three-electrode setup was used to conduct the electrochemical capability investigation of BBSDAC 700 for capacitors using electrochemical impedance spectroscopy (EIS), galvanostatic charge/discharge (GCD) testing, and cyclic voltammetry (CV) in 1 M Na_2SO_4. Fig. 4a shows that the CV curves of the BBSDAC 700 at 10 mV s^{-1} had a quasi-rectangular shape in various potential windows (between 0.0 and 1.2 V). Because the polarization of the electrode material at a high potential broke down the electrolyte, the electrode current surged dramatically. The curve's form changed when the potential window grew by more than 1.2 V. Consequently, the device's potential window was selected to be between 0 and 1.2 V. Fig. 4b shows the BBSDAC

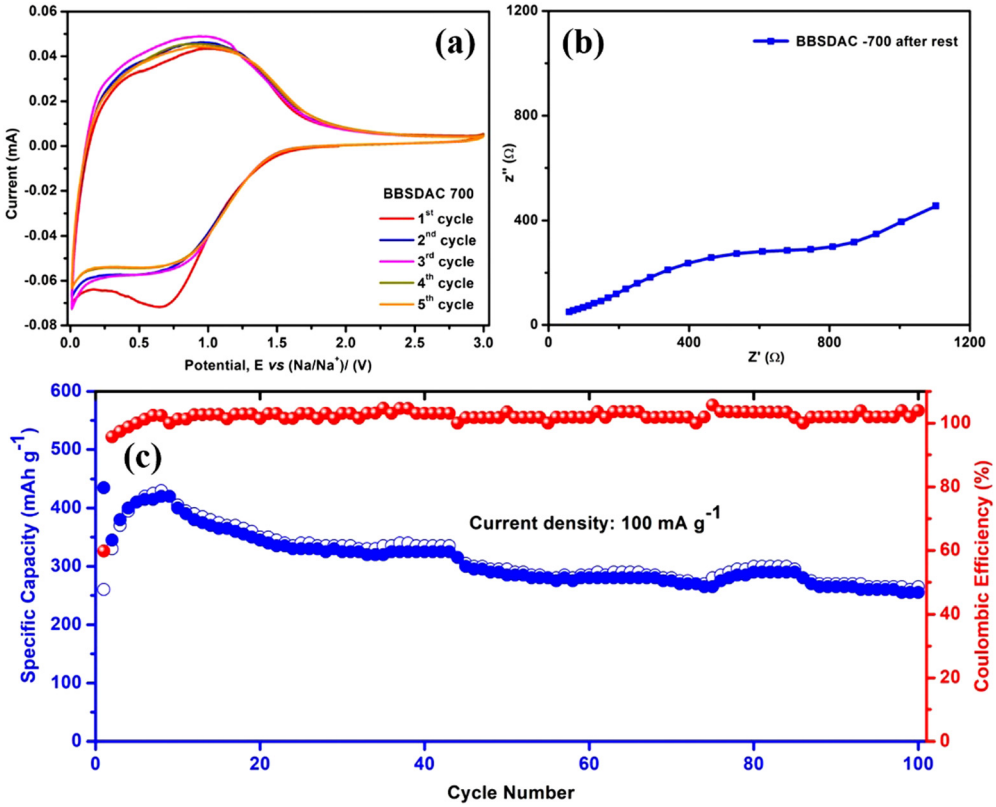

Fig. 3 (a) CV curves, (b) electrochemical impedance study, and (c) long-term cycling performance of the cell at 100 mA g^{-1} after 10 months of rest of the BBSDAC 700.

700's CVs at various sweep rates (10–500 mV s^{-1}). The curves showed that when the sweep speed increased, the BBSDAC 700's current also increased. Additionally, all CV curves had comparable quasi-rectangular forms, suggesting that the BBSDAC 700 had superior capacitance properties.[90] To gain a deeper understanding of the exceptional electrochemical performance of BBSDAC 700 as a material for supercapacitors, it is necessary to comprehend the state changes that occur throughout the cycling process as well as the reaction kinetics. We looked at the CV curves of the BBSDAC 700 electrode at various scan rates, as shown in Fig. 4b. The relationship between current (i) and scan rate (v) can be discovered using a log(i)–log(v) curve, which is typically represented as $i = av^b$. In this case, the variable constants are a and b. Whereas $b = 1$ indicates a capacitive process that is entirely in charge of charge storage, $b = 0.5$ indicates a totally diffusion-controlled process. Fig. S3 illustrates the process of calculating b values for our BBSDAC 700 electrode using the log i *vs.* log v curve. These curves have been plotted and contrasted for three voltage values—0.1 V, 0.4 V, and 1.0 V—for instructional reasons. At 0.4 V, the slope (b value) was 0.58 (nearer 0.5), indicating more intercalation/de-intercalation type charge storage. At 0.1 V and 1.0 V, the slopes (b value) were 0.88 and 0.78, respectively, indicating a capacitive charge storage mechanism with a lower diffusion-controlled contribution. The BBSDAC 700 electrode's capacitance control, also known as surface drive, appears to have a higher ratio of charge storage than diffusion control. The following formulas are used to determine the contribution from charge storage of the diffusive and capacitive types (eqn (4) and (5)).

$$i(V) = k_1 v + k_2 v^{1/2} \quad (4)$$

$$\frac{i(V)}{v^{1/2}} = k_1 v^{1/2} + k_2 \quad (5)$$

where i is the current response at a scan rate of v, and k_1 and k_2 are constants. The diffusive contribution is represented by $k_2 v^{1/2}$ and the capacitive contribution by $k_1 v$. It is possible to discern the percentage of capacitive and diffusion charge storage by looking at the plot of $\left(\frac{i(V)}{v^{1/2}}\right)$ and $v^{1/2}$ at a given potential (V) and finding the slope k_1 and Y-intercept k_2. Fig. S4 shows the percentage contribution of the BBSDAC 700 electrode at different scan rates. The fraction of capacitive contribution rises with an increase in scan rate. The GCD curves of BBSDAC 700 were acquired at 0.5–5 A g^{-1}, as illustrated in Fig. 4c. Interestingly, all curves retained a decent isosceles triangle shape even at high current densities. This outcome showed that the BBSDAC 700 had superior electrochemical reversibility and optimal supercapacitor behavior, which was in line with the findings of the CV test. High coulombic efficiency is implied by the roughly comparable charge/discharge times. The specific capacitance was calculated from the charge–discharge curves at each current density using Formula (1). With current densities of 0.5, 1, 2, 3, and 5 A g^{-1}, respectively, the specific capacitance values of BBSDAC 700 were 235, 218, 205, 184, and 129 F g^{-1}. At a current density of 1.0 A g^{-1},

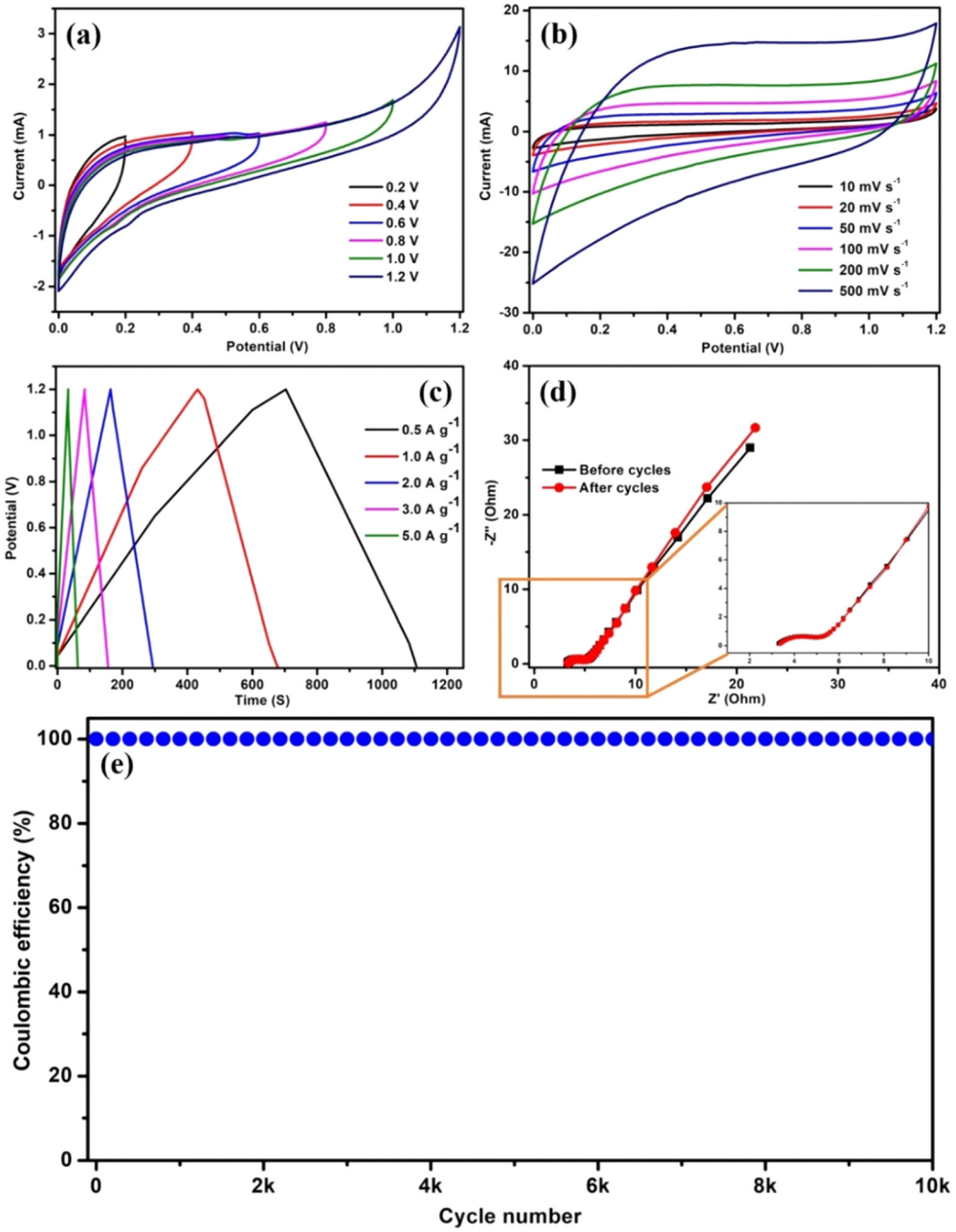

Fig. 4 Electrochemical performance of the BBSDAC 700 in 1 M Na_2SO_4 electrolyte. (a) CV curves within different potential windows from 0 to 1.2 V at 10 mV s^{-1}, (b) CV curves in a potential window between 0 and 1.2 V at various scanning rates, (c) GCD curves of the BBSDAC 700 cell at 0.5, 1.0, 2.0, 3.0 and 5.0 A g^{-1} current densities, (d) Nyquist plots of the BBSDAC 700 cell before and after cycling, and (e) capacitive retention of the BBSDAC 700 cell at the current density of 1 A g^{-1}.

a high specific capacitance of 218 F g^{-1} was detected and higher than previous reports (Table 3). It is observed that the complete usage of the electrode's active mass at low current led to a high specific capacitance. Interestingly, even at the increased current density of 5 A g^{-1}, the activated carbon electrode maintains a capacity of 129 F g^{-1}. The wide surface area of BBSDAC 700 is assumed to be the reason for the high capacitance since it enhances interaction at the electrode/electrolyte interface.

An understanding of the resistance and capacitance behavior of the capacitor may be gained from the analysis of the BBSDAC 700 EIS, which was acquired in the frequency range of 100 to 0.01 kHz. The EIS diagram for the BBSDAC 700 carbon before and after cycle life tests is displayed in Fig. 4d. Because of the electrode's stability, the charge transfer resistance did not alter even after cycling, according to EIS spectra. Furthermore, as shown in Fig. 4e, the GCD cycling stability of BBSDAC 700 was examined at 1 A g^{-1}. After 10k cycles, the capacitance stayed at about 99.5%, demonstrating no discernible capacity loss, suggesting that BBSDAC 700 exhibited exceptional cycling stability as an electrode material.

Table 3 Comparison of the electrochemical performance of BBSDAC 700 with published biomass derived carbon for SIC

Carbon source	Capacity ($F\ g^{-1}$)	Current density ($mA\ g^{-1}$)	Ref.
Corn silk	127	300	98
Cotton stalk	120	1000	99
Cork-carbon	170	100	100
Peanut shell	213	100	101
Pomelo peel	81	500	102
Tamarind pods	59	100	103
BBSDAC 700	**218**	**1000**	**This work**

Further investigation into the sample's performance in symmetric supercapacitors is required to meet the needs of real applications. A symmetrical supercapacitor was put together based on the BBSDAC 700. Fig. 5a shows that the CV curves of the BBSDAC 700 at 10 mV s^{-1} displayed a quasi-rectangular shape in various potential windows (between 0.0 and 1.4 V). The symmetric cell has an optimal potential window of 0.0–1.4 V. The scan-rate dependent CV profiles captured at different scan rates within the optimum potential window are displayed in Fig. 5b. The symmetric capacitor was tested for charge and discharge at different current densities (1 to 5 A g^{-1}) while being charged with a constant current (Fig. 5c). The data acquired for the symmetric cell are consistent with the GCD and CV curves. Using formulas (2) and (3), the symmetric capacitor device's energy and power densities were determined from the GCD profiles. Fig. 5d displays the Ragone plot that was produced. Remarkably, at a power density of 726 W kg^{-1}, the symmetric

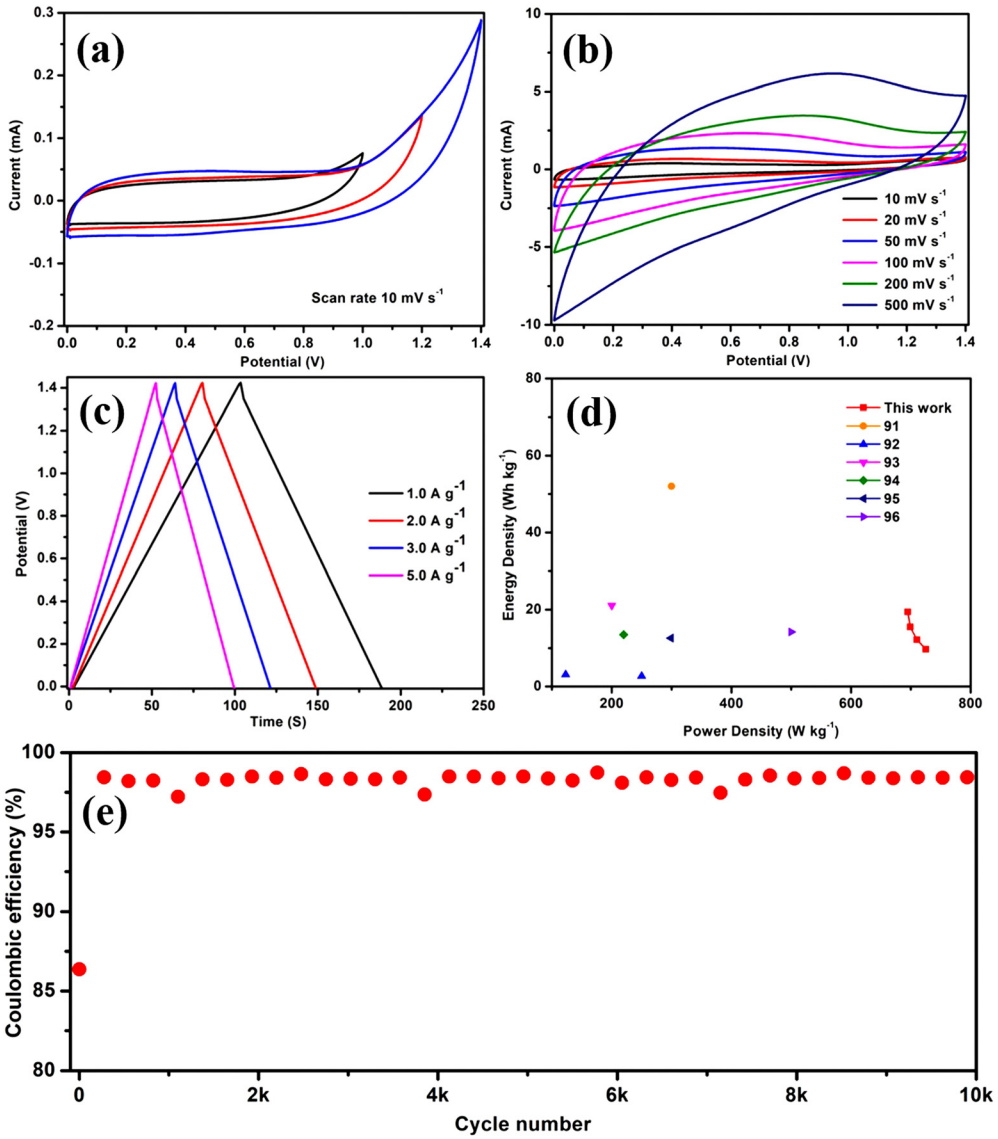

Fig. 5 Electrochemical performance of the symmetric BBSDAC 700 capacitor in 1 M Na_2SO_4 electrolyte. (a) CV curves within different potential windows from 0 to 1.4 V at 10 mV s^{-1}, (b) CV curves in a potential window between 0 and 1.4 V at various scanning rates, (c) GCD curves of the BBSDAC 700 cell at 1.0, 2.0, 3.0 and 5.0 A g^{-1} current densities, (d) Ragone plot,[92–97] and (e) cycling study of the BBSDAC 700 symmetric capacitor at the current density of 1 A g^{-1}.

capacitor shows a high energy density of 20 Wh kg^{-1}. Furthermore, as shown in Fig. 5e, the GCD cycling stability of a symmetric capacitor was investigated at 1 A g^{-1}, and after 10 000 cycles, the coulombic efficiency stayed at nearly 98%, demonstrating no discernible capacity loss. We can see that, even after hundreds of cycles, there is no capacity reduction, due to the carbon material's structural durability, the electrolyte's stability, and the absence of side reactions. According to Simone *et al.*, micropore size reduces and specific surface area (SSA) increases at low pyrolysis temperatures. In contrast to interaction/deinteraction, this event results in an increase in the surface reaction.[91] This suggests that BBSDAC 700 exhibited exceptional cycling stability as an electrode material. Both the carbon source and the process for creating the disordered material are straightforward and sustainable. Biocarbon is extremely easy to use and may be scaled up.

4. Conclusions

Carbon-based materials have garnered significant interest in batteries and supercapacitor electrodes. We could effectively synthesize BBSDAC 700 by carbonizing blackberry seeds and activating them with KOH. XRD, Raman, BET, and TEM characterization were used to study the structural evolution of the BBSDAC 700. This material has a disordered structure and a large specific surface area (604 m^2 g^{-1}). Tests were conducted on the activated BBSDAC 700 sample as the electrode material for a sodium-ion capacitor and SIB. The BBSDAC 700 delivered sodium-ion battery anode produced a high reversible capacity of 322 mAh g^{-1} at a rate of 100 mA g^{-1} with a coulombic efficiency of 99% after 200 cycles. Moreover, the BBSDAC 700 delivers a capacity of 265 mAh g^{-1} at a current density of 100 mA g^{-1} even after 10 months of rest. BBSDAC 700 has a maximum energy density of 20 Wh kg^{-1} under 1 A g^{-1} and the highest power density of 726 W kg^{-1} when used as an electrode material for a capacitor (symmetric capacitor). This finding confirmed that BBSDAC 700 carbon is a viable option for next-generation power sources because of its good electrochemical performance in SIBs and SCs.

Conflicts of interest

There are no conflicts to declare.

Data availability

The data that support the findings of this study are available from the corresponding author upon reasonable request.

Supporting information is available. Fig. S1. Nyquist plots of BBSDAC 700 before and after cycles of SIB. Fig. S2. FTIR spectrum of the BBSDAC 700 electrode even after 10 months of rest time after cycles. Fig. S3. log(i) *vs.* log(v) curves at 0.1 V, 0.4 V and 1.0 V (b-value determination) of the BBSDAC 700 electrode. Fig. S4. Percentage of the surface-controlled and diffusion-controlled area in the CV curve at different scan rate (a) 10 mV s^{-1}, (b) 20 mV s^{-1}, (c) 50 mV s^{-1}, (d) 100 mV s^{-1}, (e) 200 mV s^{-1}, and (f) 500 mV s^{-1}. See DOI: **https://doi.org/10.1039/d5ma00333d**

Acknowledgements

The authors acknowledge the financial support of this work as part of a research project PIF 726175. The authors gratefully acknowledge Alfaisal University and its Office of Research & Innovation for their continuous support throughout this study.

References

1 V. Palomares, M. Casas-Cabanas, E. Castillo-Martínez, M. H. Han and T. Rojo, *Energy Environ. Sci.*, 2013, **6**, 2312–2337.
2 T. M. I. Mahlia, T. J. Saktisahdan, A. Jannifar, M. H. Hasan and H. S. C. Matseelar, *Renewable Sustainable Energy Rev.*, 2014, **33**, 532–545.
3 B. Dunn, H. Kamath and J.-M. Tarascon, *Science*, 2011, **334**, 928–935.
4 S. W. Kim, D. H. Seo, X. H. Ma, G. Ceder and K. Kang, *Adv. Energy Mater.*, 2012, **2**, 710.
5 V. Palomares, P. Serras, I. Villaluenga, K. B. Hueso, J. Carretero-González and T. Rojo, *Energy Environ. Sci.*, 2012, **5**, 5884–5901.
6 Z. He, Y. Huang, H. Liu, Z. Geng, Y. Li, S. Li, W. Deng, G. Zou, H. Hou and X. Ji, *Nano Energy*, 2024, **129**, 109996.
7 N. Yabuuchi, K. Kubota, M. Dahbi and S. Komaba, *Chem. Rev.*, 2014, **114**, 11636–11682.
8 L. Zhao, T. Zhang, W. Li, T. Li, L. Zhang, X. Zhang and Z. Wang, *Engineering*, 2023, **24**, 172–183.
9 C. B. Tabelin, J. Dallas, S. Casanova, T. Pelech, G. Bournival, S. Saydam and I. Canbulat, *Miner. Eng.*, 2021, **163**, 106743.
10 E. Sujithkrishnan, A. Prasath, M. Govindasamy, R. A. Alshgari and P. Elumalai, *Energy Fuels*, 2021, **35**, 5320–5332.
11 X. Xiang, K. Zhang and J. Chen, *Adv. Mater.*, 2015, **27**, 5343–5364.
12 P. Vassilaras, A. J. Toumar and G. Ceder, *Electrochem. Commun.*, 2014, **38**, 79–81.
13 J. Xu, D. H. Lee, R. J. Clément, X. Yu, M. Leskes, A. J. Pell, G. Pintacuda, X.-Q. Yang, C. P. Grey and Y. S. Meng, *Chem. Mater.*, 2014, **26**, 1260–1269.
14 H. Yu, S. Guo, Y. Zhu, M. Ishida and H. Zhou, *Chem. Commun.*, 2014, **50**, 457–459.
15 V. P. Mhaske and M. D. Yadav, *Chem. Eng. Sci.*, 2024, **295**, 120177.
16 T. Cui, X. Li, Y. Si and Y. Fu, *Energy Storage Mater.*, 2024, **65**, 103161.
17 M. Pan, Y. Wang, Y. Liu, M. Zhang, X. Liu, Y. Yuan, Y. Zhou, W. Liu, T. Chen and K. Liu, *Chem. Eng. J.*, 2024, **495**, 153396.
18 R. S. Kate, H. S. Jadhav, U. P. Chothe, K. Bhattacharjee, M. V. Kulkarni, R. J. Deokate, B. B. Kale and R. S. Kalubarme, *J. Mater. Chem. A*, 2024, **12**, 7418–7451.
19 T. Ouaneche, L. Stievano, L. Monconduit, C. Guéry, M. T. Sougrati and N. Recham, *Batteries Supercaps*, 2024, **7**, e202400214.

20 Y. Shmatok, N. Globa, V. Sirosh and S. Kirillov, *ChemNanoMat*, 2024, **10**, e202400065.
21 T. Meng, Z. Chen, X. Lai, J. Xing, C. Chen and D. Sun, *Small*, 2024, 2405822.
22 M. Yang, K. Wang, Q. Liu, S. Cao, J. Wang and Y. Liu, *J. Alloys Compd.*, 2024, **973**, 172899.
23 A. Rützler, J. Büttner, J. Oechsler, S. E. Balaghi, S. Küspert, N. Ortlieb and A. Fischer, *Adv. Funct. Mater.*, 2024, **34**, 2401188.
24 D. Wu, Y. Huang and X. Hu, *Chem. Commun.*, 2016, **52**, 11207–11210.
25 C. Liu, X. Fu, S. Liao, G. Zou and H. Yang, *Nanomaterials*, 2023, **13**(2), 254.
26 J. Płotek, A. Kulka, A. Maximenko, Ł. Kondracki, S. Trabesinger, M. Moździerz, P. Czaja and J. Molenda, *Energy Storage Mater.*, 2024, **72**, 103780.
27 N. Regragui, Z. Mansouri, A. Al-Shami, O. Mounkachi and H. Ez-Zahraouy, *J. Energy Storage*, 2024, **97**, 112886.
28 J. Liang, C. Wei, D. Huo and H. Li, *J. Energy Storage*, 2024, **85**, 111044.
29 Y. Chen, Z. Dong, S. Lai, Y. Li, W. Lv, Y.-B. He, F. Kang and M. Liu, *Adv. Funct. Mater.*, 2024, **34**(48), 2408657.
30 A. K. Prajapati and A. Bhatnagar, *J. Energy Chem.*, 2023, **83**, 509–540.
31 Y. Chen, H. Sun, X.-X. He, Q. Chen, J.-H. Zhao, Y. Wei, X. Wu, Z. Zhang, Y. Jiang and S.-L. Chou, *Small*, 2024, **20**, 2307132.
32 D. Zhang, G. Huang, H. Zhang, Z. Zhang, Y. Liu, F. Gao, Z. Shang, C. Gao, Y. Zhou, S. Fu, J. Wei, M. Terrones and Y. Wang, *Chem. Eng. J.*, 2024, **495**, 153646.
33 X. Sun, X. Gao, Z. Li, X. Zhang, X. Zhai, Q. Zhang, L. Li, N. Gao, G. He and H. Li, *Small Methods*, 2024, **8**, 2300746.
34 J. Xie, R. Zhuang, Y. Du, Y. Pei, D. Tan and F. Xu, *New Carbon Mater.*, 2023, **38**, 305–316.
35 X.-Y. Wang, K.-Y. Zhang, M.-Y. Su, H.-H. Liu, Z.-Y. Gu, D. Dai, B. Li, J.-W. Wang, X.-Y. He and X.-L. Wu, *Carbon*, 2024, **229**, 119526.
36 B. Yan, C. Han, Y. Dai, M. Li, Z. Wu and X. Gao, *Fuel*, 2024, **371**, 132141.
37 Z. Li, L. Yu, X. Tao, Y. Li, L. Zhang, X. He, Y. Chen, S. Xiong, W. Hu, J. Li, J. Wang, H. Jin and S. Wang, *Small*, 2024, **20**, 2304124.
38 N. T. T. Hoa, N. V. Ky, L. T. Son, D. T. Dung, T. V. Nguyen, V. D. Lam and N. V. Nghia, *J. Electroanal. Chem.*, 2023, **929**, 117129.
39 N. Voronina, J. H. Yu, H. J. Kim, N. Yaqoob, O. Guillon, H. Kim, M.-G. Jung, H.-G. Jung, K. Yazawa, H. Yashiro, P. Kaghazchi and S.-T. Myung, *Adv. Funct. Mater.*, 2023, **33**, 2210423.
40 H. Wang, R. Qian, Y. Cheng, H.-H. Wu, X. Wu, K. Pan and Q. Zhang, *J. Mater. Chem. A*, 2020, **8**, 18425–18463.
41 Y. Huang, X. Li, J. Luo, K. Wang, Q. Zhang, Y. Qiu, S. Sun, S. Liu, J. Han and Y. Huang, *ACS Appl. Mater. Interfaces*, 2017, **9**, 8696–8703.
42 K. Xu, J. Xie, H. Dong, C. Sun, Y. Li, J. Guo, Z. Wang, J. Yang and H. Geng, *J. Colloid Interface Sci.*, 2024, **656**, 241–251.
43 Z. Wang, H. Yang, Y. Liu, Y. Bai, G. Chen, Y. Li, X. Wang, H. Xu, C. Wu and J. Lu, *Small*, 2020, **16**, 2003268.
44 R. Qiu, D. Ma, H. Zheng, M. Liu, J. Cai, W. Yan and J. Zhang, *Nano Energy*, 2024, **128**, 109920.
45 L. Lyu, Y. Yi and Z.-L. Xu, *Batteries Supercaps*, 2025, **8**(3), e202400521.
46 G. Åvall, M. Goktas and P. Adelhelm, *Sodium-Ion Batteries*, John Wiley & Sons, Ltd, 2022, pp. 1–25.
47 C. Senthil, J. W. Park, N. Shaji, G. S. Sim and C. W. Lee, *J. Energy Chem.*, 2022, **64**, 286–295.
48 Y. Sun, X.-L. Shi, Y.-L. Yang, G. Suo, L. Zhang, S. Lu and Z.-G. Chen, *Adv. Funct. Mater.*, 2022, **32**, 2201584.
49 W. Nie, X. Liu, Q. Xiao, L. Li, G. Chen, D. Li, M. Zeng and S. Zhong, *ChemElectroChem*, 2020, **7**, 631–641.
50 L. Wu, D. Buchholz, C. Vaalma, G. A. Giffin and S. Passerini, *ChemElectroChem*, 2016, **3**, 292–298.
51 M. Thenappan, S. Rengapillai and S. Marimuthu, *Energies*, 2022, **15**(21), 8086.
52 Y. Tang, J. He, J. Peng, J. Yang, Z. Wu, P. Liu, K. Zhou, S. Hu, L. Hu and X. Wang, *Energy Fuels*, 2024, **38**, 7389–7398.
53 X. Zhang, J. Hu, X. Chen, M. Zhang, Q. Huang, X. Du, Y. Liu and X. Li, *J. Porous Mater.*, 2019, **26**, 1821–1830.
54 C. Ma, H. Wang, X. Zhao, X. Wang, Y. Miao, L. Cheng, C. Wang, L. Wang, H. Yue and D. Zhang, *Energy Technol.*, 2020, **8**, 1901445.
55 Y. Li, Y. Lu, Q. Meng, A. C. S. Jensen, Q. Zhang, Q. Zhang, Y. Tong, Y. Qi, L. Gu, M.-M. Titirici and Y.-S. Hu, *Adv. Energy Mater.*, 2019, **9**, 1902852.
56 E. Gibertini, F. Liberale, C. Dossi, G. Binda, B. Mattioli, R. Bettinetti, A. Maspero, M. Fiore, R. Ruffo and L. Magagnin, *J. Appl. Electrochem.*, 2021, **51**, 1665–1673.
57 A. V. Baskar, G. Singh, A. M. Ruban, J. M. Davidraj, R. Bahadur, P. Sooriyakumar, P. Kumar, A. Karakoti, J. Yi and A. Vinu, *Adv. Funct. Mater.*, 2023, **33**, 2208349.
58 X. Meng, P. E. Savage and D. Deng, *Environ. Sci. Technol.*, 2015, **49**, 12543–12550.
59 H. Darjazi, A. Staffolani, L. Sbrascini, L. Bottoni, R. Tossici and F. Nobili, *Energies*, 2020, **13**(23), 6216.
60 E. O. Ajala, J. O. Ighalo, M. A. Ajala, A. G. Adeniyi and A. M. Ayanshola, *Bioresour. Bioprocess.*, 2021, **8**, 87.
61 T. K. Kumaresan, S. A. Masilamani, K. Raman, S. Z. Karazhanov and R. Subashchandrabose, *Electrochim. Acta*, 2021, **368**, 137574.
62 H. Chen, N. Sun, Y. Wang, R. A. Soomro and B. Xu, *Energy Storage Mater.*, 2023, **56**, 532–541.
63 P. Tsai, S.-C. Chung, S. Lin and A. Yamada, *J. Mater. Chem. A*, 2015, **3**, 9763–9768.
64 Y. Li, Z. Li, B. Xing, H. Li, Z. Ma, W. Zhang, P. Reubroycharoen and S. Wang, *J. Anal. Appl. Pyrolysis*, 2021, **155**, 105072.
65 Y. Yao, T. Xie, P. Li, W. Du, J. Jiang, H. Ding, T. Zhao, G. Xu and L. Zhang, *Diamond Relat. Mater.*, 2023, **138**, 110169.
66 R. Thangavel, K. Kaliyappan, K. Kang, X. Sun and Y.-S. Lee, *Adv. Energy Mater.*, 2016, **6**, 1502199.
67 S. Payá, N. Díez and M. Sevilla, *Sustainable Energy Fuels*, 2023, **7**, 2378–2389.
68 U. Choe, Y. Li, L. Yu, B. Gao, T. T. Wang, J. Sun, P. Chen and L. Yu, *Food Sci. Nutr.*, 2020, **8**, 1215–1225.

69 J. Wang, P. Lian, Q. Yu, J. Wei and W. Kang, *Food Nutr. Res.*, 2017, **61**, 1379862.
70 R. Verma, T. Gangrade, R. Punasiya and C. Ghulaxe, *Pharmacogn. Rev.*, 2014, **8**, 101.
71 A. Hameed, M. Galli, E. Adamska-Patruno, A. Krętowski and M. Ciborowski, *Nutrients*, 2020, **12**, 2538.
72 V. Yang, R. A. Senthil, J. Pan, A. Khan, S. Osman, L. Wang, W. Jiang and Y. Sun, *J. Electroanal. Chem.*, 2019, **855**, 113616.
73 C. Zhao, Q. Wang, Y. Lu, B. Li, L. Chen and Y.-S. Hu, *Sci. Bull.*, 2018, **63**, 1125–1129.
74 J. Shu, S. Cheng, H. Xia, L. Zhang, J. Peng, C. Li and S. Zhang, *RSC Adv.*, 2017, **7**, 14395–14405.
75 F. Wu, J. Bai, J. Feng and S. Xiong, *Nanoscale*, 2015, **7**, 17211–17230.
76 M. Du, Y. Meng, C. Wang, C. Duan, F. Zhu and Y. Zhang, *J. Electroanal. Chem.*, 2019, **834**, 17–25.
77 F. Li, W. Liu, Y. Lai, F. Qin, L. Zou, K. Zhang and J. Li, *J. Alloys Compd.*, 2017, **695**, 1743–1752.
78 H. Wan and X. Hu, *Int. J. Hydrogen Energy*, 2019, **44**, 22250–22262.
79 D. Qin, F. Zhang, S. Dong, Y. Zhao, G. Xu and X. Zhang, *RSC Adv.*, 2016, **6**, 106218–106224.
80 L. Fu, K. Tang, K. Song, P. A. van Aken, Y. Yu and J. Maier, *Nanoscale*, 2014, **6**, 1384–1389.
81 S. X. L. Guo, Y. An, H. Fei, J. Feng and L. Ci, *Mater. Technol.*, 2017, **32**, 592–597.
82 P. Wang, B. Qiao, Y. Du, Y. Li, X. Zhou, Z. Dai and J. Bao, *J. Phys. Chem. C*, 2015, **119**, 21336–21344.
83 Z. Yan, Q.-W. Yang, Q. Wang and J. Ma, *Chin. Chem. Lett.*, 2020, **31**, 583–588.
84 Y. Li, Y.-S. Hu, M.-M. Titirici, L. Chen and X. Huang, *Adv. Energy Mater.*, 2016, **6**, 1600659.
85 H. Wang, H. Chen, C. Chen, M. Li, Y. Xie, X. Zhang, X. Wu, Q. Zhang and C. Lu, *Chin. Chem. Lett.*, 2023, **34**, 107465.
86 Y. Shen, S. Sun, M. Yang and X. Zhao, *J. Alloys Compd.*, 2019, **784**, 1290–1296.
87 L. A. Middlemiss, A. J. R. Rennie, R. Sayers and A. R. West, *J. Electrochem. Soc.*, 2024, **171**, 010528.
88 X. Shu, Y. Li, B. Yang, Q. Wang and K. Punyawudho, *Molecules*, 2024, **29**(20), 4963.
89 B. Kishore, L. Chen, C. E. J. Dancer and E. Kendrick, *Chem. Commun.*, 2020, **56**, 12925–12928.
90 Md Akib Hasan, S. Sayantha Aniv and Md Mominul Islam, *Chem. Rec.*, 2024, **24**, e202300153.
91 V. Simone, A. Boulineau, A. de Geyer, D. Rouchon, L. Simonin and S. Martinet, *J. Energy Chem.*, 2016, **25**, 761–768.
92 S. Wang, R. Wang, Y. Zhang, D. Jin and L. Zhang, *J. Power Sources*, 2018, **379**, 33–40.
93 O. C. Altinci and M. Demir, *Energy Fuels*, 2020, **34**, 7658–7665.
94 J. Abdulsalam, K. Otun, N. Gardee, B. Patel, T. Leswifi and M. K. Mathe, *ACS Omega*, 2023, **8**, 5285–5299.
95 G. Ma, J. Li, K. Sun, H. Peng, E. Feng and Z. Lei, *J. Solid State Electrochem.*, 2017, **21**, 525–535.
96 H. Gege, W. Ying, Z. Tianyun, W. Xingxing and C. Jinjun, *J. Taiwan Inst. Chem. Eng.*, 2019, **96**, 672–680.
97 U. Thubsuang, S. Laebang, N. Manmuanpom, S. Wongkasemjit and T. Chaisuwan, *J. Mater. Sci.*, 2017, **52**, 6837–6855.
98 M. Vadivazhagan, P. Parameswaran, U. Mani and K. Nallathamby, *ACS Sustainable Chem. Eng.*, 2018, **6**, 13915–13923.
99 J. Chen, X. Zhou, C. Mei, J. Xu, S. Zhou and C.-P. Wong, *J. Power Sources*, 2017, **342**, 48–55.
100 M. D. Casal, N. Díez, S. Payá and M. Sevilla, *ACS Appl. Energy Mater.*, 2023, **6**, 8120–8131.
101 J. Ding, H. Wang, Z. Li, K. Cui, D. Karpuzov, X. Tan, A. Kohandehghan and D. Mitlin, *Energy Environ. Sci.*, 2015, **8**, 941–955.
102 N. T. Nguyen, P. A. Le and V. B. T. Phung, *J. Nanopart. Res.*, 2020, **22**, 371.
103 V. Thirumal, T. V. M. Sreekanth, K. Yoo and J. Kim, *Energies*, 2023, **16**(2), 802.